Journal of Computational Mathematics
Vol.28, No.3, 2010, 354–370.

http://www.global-sci.org/jcm
doi:10.4208/jcm.2009.12-m1001

SEPARATION OF SCALES IN ELASTICITY IMAGING: A NUMERICAL STUDY*

Habib Ammari
Institut Langevin, Laboratoire Ondes et Acoustique, CNRS UMR 7587, ESPCI, 10 rue Vauquelin, 75231 Paris Cedex 05, France
Email: habib.ammari@espci.fr
Pierre Garapon and François Jouve
Laboratoire J.L. Lions, Université Paris VII, Denis Diderot, 75252 Paris, France
Email: pierre.garapon@espci.fr, jouve@math.jussieu.fr

Abstract

In magnetic resonance elastography, one seeks to reconstruct the shear modulus from measurements of the displacement field in the whole body. In this paper, we present an optimization approach which solves the problem by simply minimizing a discrepancy functional. In order to recover a complex anomaly in a homogenous medium, we first observe that the information contained in the wavefield should be decomposed into two parts, a "near-field" part in the region around the anomaly and a "far-field" part in the region away from the anomaly. As will be justified both theoretically and numerically, separating these scales provides a local and precise reconstruction.

Mathematics subject classification: 35R30,74L15,92C55.
Key words: Elastography, multi-scale imaging, anomaly reconstruction.

1. Introduction

Extensive work has been carried out in the past decade to image the elastic properties of human soft tissues by inducing motion. This broad field, called elasticity imaging or elastography, is based on the initial idea that shear elasticity can be correlated with the pathology of tissues.

There are several techniques that can be classified according to the type of mechanical excitation chosen (static compression, monochromatic, or transient vibration) and the way these excitations are generated (externally or internally). Different imaging modalities can be used to estimate the resulting tissue displacements.

Magnetic resonance elastography (MRE) is a new way of applying the idea of elastography. It can directly visualize and quantitatively measure the displacement field in tissues subject to harmonic mechanical excitation at low-frequencies.

The principle of the MRE relies on three steps: first applying dynamic shear to a tissue, then measuring displacement, and finally solving an inverse problem to get a map of Young's modulus. Each one of these three steps is a technical challenge by itself. The works [2, 9, 18] describe various frameworks of this problem. We will focus on the so called "steady state" elastography, whose principles have been described in [16], and more recently in [18]. A harmonic excitation is applied by vibrating a piezoelectric transducer onto the body. This vibration

* Received April 13, 2009 / Revised version received June 11, 2009 / Accepted June 12, 2009 / Published online February 1, 2010 /

propagates in the tissue and thus produces a harmonic displacement field. Figure 1.1 shows the modulus of the complex amplitude of such a displacement field obtained experimentally. The displacement field is imaged in the whole volume by a specific sequence of Magnetic Resonance Imaging (MRI). Such a sequence is called an elastography sequence. Once this displacement is acquired, an inverse problem is used to reconstruct the shear modulus. Being able to image the displacement in the whole volume is a crucial feature of the technique because it gives much more detailed information than what can be obtained from boundary measurements. As we will explain in this paper, such an imaging system has better resolution.

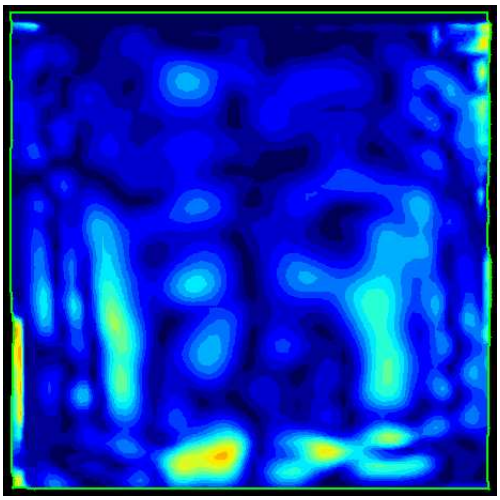

Fig. 1.1. Experimental wavefield in a phantom. The displacement field is acquired by an MRI sequence (R. Sinkus's group – LOA). The transducer is at the bottom. Although the waves are visible, the amplitude decays in the vertical direction because of a viscosity in the tissue.

We want to numerically estimate the local stiffness of the medium, given the displacement field produced by a known excitation. In this paper, we discuss the resolution performance one could expect when solving this kind of inverse problems with interior measurements.

The inverse problem for elastography is investigated in many different ways depending on the experimental setup. In MRE, it is common to solve the inverse problem by estimating the derivatives of the displacement field using finite different schemes; see for instance [17] and Section 2. Other contributors suggested to use finite element methods to match the displacement field; see, e.g., [20] and [19]. Our approach is somehow similar to this paradigm. We propose here a mathematical interpretation of the results. Indeed, our numerical simulation tool is different.

The paper is organized as follows. In Section 2, we recall our mathematical model for steady state elastography, and describe our optimization approach to solve the inverse problem. In Section 3, we investigate the resolution limits of our approach by considering a specific set of discontinuous coefficients to be recovered. In Section 4, we summarize the advantages and the disadvantages of our method by considering issues of stability, accuracy and computational performance.

2. The Inverse Problem of Elastography

2.1. Mathematical model

As previously said, elastography consists mainly of two steps: inducing a displacement in a soft medium, and solving an inverse problem in order to estimate the stiffness of the tissue. Depending on the experimental framework, various mathematical models can be used to describe the problem: some are based on the anisotropy of the tissues such as muscle or brain [7] and others are based on the dissipation of the mechanical energy in tissues such as liver [10]. However, we make the same assumptions that are common in the elastography community and choose to study a linear, isotropic elastic medium, without any dissipation. Moreover, as soft tissues are incompressible we use the incompressible elasticity model derived in [4].

Let Ω be a smooth domain in $\mathbb{R}^2$, and let its boundary be the union of two disjoint components $\partial\Omega = \Gamma_1 \cup \Gamma_2$. Let ν denote the outward unit normal to $\partial\Omega$. Consider the pair $(\mathbf{u}, p) \in (H^1)^2 \times L^2$ to be the solution to the following system:

$$\begin{cases} \nabla \cdot (\mu \mathbf{e}(\mathbf{u})) + \rho\omega^2 \mathbf{u} + \nabla p = 0 \quad \text{in} \quad \Omega, \\ \nabla \cdot \mathbf{u} = 0 \quad \text{in} \quad \Omega, \\ \mathbf{u} = F \quad \text{on} \quad \Gamma_1, \\ p\nu + \mu \mathbf{e}(\mathbf{u})\nu = 0 \quad \text{on} \quad \Gamma_2, \end{cases} \tag{2.1}$$

where $\mathbf{e}(\mathbf{u}) = \frac{1}{2}(\nabla \mathbf{u} + \nabla \mathbf{u}^t)$ is the strain tensor (t stands for transpose).

One can interpret this system as follows: $\mathbf{u}$ is the displacement field in the medium, μ is the shear modulus or the stiffness of the medium, ρ is the density of the medium, ω is the pulsation of the excitation applied on the boundary, p is the pressure field in the medium, the boundary conditions correspond to the part of the boundary Γ_2 which is free, and to the part Γ_1 of the boundary where the mechanical excitation is imposed. As shown in [4], this system is actually the limiting system of the compressible Lamé system, where the compression modulus λ goes to $+\infty$.

It is known that, except for a discrete number of values of ω, $\mathbf{u} = 0$ if $F = 0$. See for instance [13].

2.2. Definition of the inverse problem

The problem can be described in the following form: suppose we have at our disposal a medium of shape Ω, with shear modulus μ^*, which is not known. We impose the boundary conditions described above, and thus in the medium, a displacement field $\mathbf{u}_{\text{exp}}$ and a pressure field p_{exp} appear. They are solution to (2.1). We measure the displacement field $\mathbf{u}_{\text{exp}}$ (hence it is known). The inverse problem consists in estimating μ^* from the information provided by $\mathbf{u}_{\text{exp}}$. The following estimation:

$$\mu = -\frac{\rho\omega^2 \mathbf{q}}{\Delta \mathbf{q}}, \quad \mathbf{q} = \nabla \times \mathbf{u}_{\text{exp}}$$

has been suggested in [17, 18]. It gives the value of the shear modulus at every point as a function of the values of the derivatives of the displacement field. It is an approximation that is valid as long as the shear modulus varies smoothly. Consequently, it is impractical to use it to reconstruct interfaces and anomalies. Moreover, in concrete situations $\mathbf{u}_{\text{exp}}$ is measured

experimentally and is therefore noisy. The computation of its derivatives is unstable and this technique, although quite efficient, requires smoothing and fine tuning of a certain number of parameters.

In this paper, we suggest solving this inverse problem numerically by an optimization approach. We have a numerical simulation tool that allows us to solve the so-called direct problem. If we assume a shear modulus distribution μ to be the correct one, we can compute the numerical solution $\mathbf{u}_{\text{mod}}(\mu)$ of problem (2.1). An intuitive criterion for an estimated map μ is wether $\mathbf{u}_{\text{mod}}(\mu)$ is similar to $\mathbf{u}_{\text{exp}}$, since we want μ to be such that those two displacement fields look as alike as possible. From a mathematical point of view, we want to numerically minimize, with respect to the shear modulus map μ, the discrepancy functional:

$$J(\mu) = \frac{1}{2}||\mathbf{u}_{\text{exp}} - \mathbf{u}_{\text{mod}}(\mu)||_2^2.$$

The computed minimizer will be our estimator $\tilde{\mu}$. Actually, if we want $\mathbf{u}_{\text{mod}}$ and $\mathbf{u}_{\text{exp}}$ to be alike, we should impose the conditions that match perfectly on the boundary $\partial\Omega$. From now on, $\mathbf{u}_{\text{mod}}$ will denote the solution to the following problem:

$$\begin{cases} \nabla \cdot (\mu(x)\mathbf{e}(\mathbf{u})) + \rho\omega^2\mathbf{u} + \nabla p = 0 \quad \text{in} \quad \Omega, \\ \nabla \cdot \mathbf{u} = 0 \quad \text{in } \Omega, \\ \mathbf{u} = \mathbf{u}_{\text{exp}} \quad \text{on} \quad \partial\Omega. \end{cases} \tag{2.2}$$

The discrepancy functional will be as follows:

$$J(\mu) = \frac{1}{2}||\mathbf{u}_{\text{exp}} - \mathbf{u}_{\text{mod}}(\mu)||_2^2,$$

where $\mathbf{u}_{\text{mod}}(\mu)$ is the solution of (2.2) and $\mathbf{u}_{\text{exp}}$ is a field being observed (the result of an experiment or of a numerical simulation in our case), and which does not depend on μ.

2.3. Optimization of the discrepancy functional

In order to minimize the discrepancy functional, we adopt a simple gradient descent method. To do this, we need to compute the derivatives of the discrepancy functional with respect to μ. Then, starting from an initial guess for the shear modulus map, μ_0, we evolve the map μ with the following dynamics:

$$\frac{\partial \mu}{\partial t} = -\frac{\partial J}{\partial \mu},$$

which we discretize, and then use to obtain the following update procedure:

$$\begin{cases} \text{initial guess } \mu_0, \\ \mu_{n+1} = \mu_n - \delta \dfrac{\partial J}{\partial \mu}(\mu_n). \end{cases} \tag{2.3}$$

Here, δ is an update parameter, which we will determine. The computed minimizer will be our estimator $\tilde{\mu}$, that is

$$\lim_{n\to\infty} \mu_n = \tilde{\mu}.$$

Notice that we have here a numerical understanding of the estimator. We did not treat the question wether μ_n converges to the actual shear modulus map μ^*, and at which speed; see in this connection [12]. Rather we are interested in the interpretation of the numerical estimator $\tilde{\mu}$ that we will build.

Numerical evidence provided later in this paper (Figures 2.1 and 2.2) shows that the convergence is efficient.

The purpose of this paper is to illustrate the intrinsic limitations of such an optimization technique, namely the scale coupling (cf. Section 3) and the stability issues (cf. Section 4).
In order to compute the derivatives of the functional J, we use an adjoint based method. To begin, we first need to derive a variational formulation for problem (2.1). Let $\tilde{\mathbf{u}} \in H^{\frac{1}{2}}(\partial\Omega)$ be the trace of $\mathbf{u}_{\text{exp}}$ on the boundary of Ω. There exists $\tilde{\mathbf{v}} \in (H^1(\Omega))^2$ such that $\nabla \cdot \tilde{\mathbf{v}} = 0$ in Ω and $\tilde{\mathbf{v}} = \tilde{\mathbf{u}}$ on $\partial\Omega$; see [8]. Indeed, one keeps in mind that as $\mathbf{u}_{\text{exp}}$ is divergence-free, the mean of the normal component of its trace over the boundary $\partial\Omega$ is 0. Let $\mathbf{v}$ be a solution of (2.2), $\mathbf{h} = \mathbf{v} - \mathbf{u}_{\text{exp}}$ is in $(H_0^1(\Omega))^2$ and satisfies the following system:

$$\begin{cases} \nabla \cdot (\mu(x)\mathbf{e}(\mathbf{h})) + \rho\omega^2\mathbf{h} + \nabla p = \tilde{\mathbf{f}} \quad \text{in} \quad \Omega, \\ \nabla \cdot \mathbf{h} = 0 \quad \text{in} \quad \Omega, \\ \mathbf{h} = 0 \quad \text{on} \quad \partial\Omega, \end{cases} \tag{2.4}$$

where $\tilde{\mathbf{f}} = \nabla \cdot (\mu(x)\mathbf{e}(\mathbf{u}_{\text{exp}})) + \rho\omega^2\mathbf{u}_{\text{exp}}$. Because $\mathbf{u}_{rmexp}$ is in H^1, one can prove that $\tilde{\mathbf{f}}$ is in H^{-1} and thus problem (2.4) has a solution in H^1. Notice that $\tilde{\mathbf{f}}$ is linear in μ as $\mathbf{u}_{\text{exp}}$ does not depend on μ. Thus the variational formulation of (2.4) is (see [8]): find $\mathbf{h} \in H_{\text{div}}$ such that

$$-\int_\Omega \mu\ \mathbf{e}(\mathbf{h}) : \mathbf{e}(\mathbf{v}) + \rho\omega^2\mathbf{h}.\mathbf{v}dx = \int_\Omega \tilde{f}.\mathbf{v}\ dx, \quad \forall \mathbf{v} \in H_{\text{div}}.$$

Here, $H_{\text{div}} = \{f \in (H_0^1)^2, \nabla \cdot f = 0\}$ and $\mathbf{e}(\mathbf{h}) = \frac{1}{2}(\nabla\mathbf{h} + \nabla\mathbf{h}^t)$. If $\mathbf{a}$ and $\mathbf{b}$ are matrices, by $\mathbf{a} : \mathbf{b}$ we denote $\mathbf{a}_{ij}\mathbf{b}_{ij}$. For a given medium μ, let us denote the solution of (2.4) by $\hat{\mathbf{u}}_{\text{mod}}$ so that $\hat{\mathbf{u}}_{\text{mod}} = \mathbf{u}_{\text{mod}} - \tilde{\mathbf{v}}$. Now let us write a modified discrepancy functional:

$$\tilde{J}(\mu, \mathbf{h}, \mathbf{v}) = \frac{1}{2}||\mathbf{u}_{\text{exp}} - \mathbf{h} - \tilde{\mathbf{v}}||_2^2 - \int_\Omega \mu\ \mathbf{e}(\mathbf{h}) : \mathbf{e}(\mathbf{v}) + \rho\omega^2\mathbf{h}.\mathbf{v}dx - \int_\Omega \tilde{f}.\mathbf{v}\ dx.$$

The relationship between J and $\tilde{J}$ is given by

$$\forall \mathbf{v} \in H_{\text{div}} \quad J(\mu) = \tilde{J}(\mu, \hat{\mathbf{u}}_{\text{mod}}(\mu), \mathbf{v}), \quad \hat{\mathbf{u}}_{\text{mod}} \text{ satisfies (2.4)}.$$

If one differentiates with respect to μ this identity, then one finds:

$$\frac{\partial J}{\partial \mu} = \frac{\partial \tilde{J}}{\partial \mu}(\mu, \hat{\mathbf{u}}_{\text{mod}}, \mathbf{v}) + \frac{\partial \tilde{J}}{\partial \mathbf{h}}(\mu, \hat{\mathbf{u}}_{\text{mod}}, \mathbf{v}) \cdot \frac{\partial \mathbf{u}_{\text{mod}}}{\partial \mu}, \quad \hat{\mathbf{u}}_{\text{mod}} \text{ satisfies (2.4)}.$$

This equality holds for all $\mathbf{v} \in H_{\text{div}}$, and thus in particular for $\mathbf{v}_0$ such that $\frac{\partial \tilde{J}}{\partial \mathbf{h}}(\mu, \hat{\mathbf{u}}_{\text{mod}}, \mathbf{v}_0) \equiv 0$. Notice that this is a linear form in H_{div}^* being 0. Hence the derivative is defined by:

$$\begin{cases} \dfrac{\partial J}{\partial \mu} = \dfrac{\partial \tilde{J}}{\partial \mu}(\mu, \hat{\mathbf{u}}_{\text{mod}}, \mathbf{v}_0), \\ \forall \mathbf{v} \in H_{\text{div}}, \quad -\displaystyle\int_\Omega \mu\ \mathbf{e}(\hat{\mathbf{u}}_{\text{mod}}) : \mathbf{e}(\mathbf{v}) + \rho\omega^2\hat{\mathbf{u}}_{\text{mod}}.\mathbf{v}dx = \int_\Omega \tilde{f}.\mathbf{v}\ dx, \\ \dfrac{\partial \tilde{J}}{\partial \mathbf{h}}(\mu, \hat{\mathbf{u}}_{\text{mod}}, \mathbf{v}_0) \equiv 0, \end{cases} \tag{2.5}$$

or equivalently,

$$\begin{cases} \dfrac{\partial J}{\partial \mu} = -\mathbf{e}(\mathbf{u}_{\text{mod}}) : \mathbf{e}(\mathbf{v}_0), \\ \forall \mathbf{v} \in H_{\text{div}}, \quad -\displaystyle\int_\Omega \mu\ \mathbf{e}(\hat{\mathbf{u}}_{\text{mod}}) : \mathbf{e}(\mathbf{v}) + \rho\omega^2\hat{\mathbf{u}}_{\text{mod}}.\mathbf{v}dx = \int_\Omega \tilde{f}.\mathbf{v}\ dx, \\ \forall \mathbf{w} \in H_{\text{div}}, \quad \displaystyle\int_\Omega (\mathbf{u}_{\text{exp}} - \hat{\mathbf{u}}_{\text{mod}} - \tilde{\mathbf{v}}) \cdot \mathbf{w} - \int_\Omega \mu\ \mathbf{e}(\mathbf{w}) : \mathbf{e}(\mathbf{v}_0) + \rho\omega^2\mathbf{w}.\mathbf{v}_0 dx = 0. \end{cases} \tag{2.6}$$

The last equation means that $\mathbf{v}_0$ is the solution of the so-called adjoint problem. Although, this variational formulation corresponds to the equation we solve numerically, we can give a strong form of this equation. If Ω is smooth and simply connected, then $\nabla \cdot (\mu(x)\mathbf{e}(\mathbf{v}_0)) + \rho\omega^2\mathbf{v}_0 + (\mathbf{u}_{\text{exp}} - \mathbf{u}_{\text{mod}})$ which is in H^{-1} and in the polar of H_{div}, can be represented as the gradient of a scalar field p^* in L^2. Thus the strong form of the adjoint problem is

$$\begin{cases} \nabla \cdot (\mu(x)\mathbf{e}(\mathbf{v}_0)) + \rho\omega^2\mathbf{v}_0 + \nabla p^* = -(\mathbf{u}_{\text{exp}} - \mathbf{u}_{\text{mod}}) \quad \text{in} \quad \Omega, \\ \nabla \cdot \mathbf{v}_0 = 0 \quad \text{in} \quad \Omega, \\ \mathbf{v}_0 = 0 \quad \text{on} \quad \partial\Omega. \end{cases} \tag{2.7}$$

2.4. Numerical Implementation

Provided we have a numerical tool to solve direct and adjoint problems, we can compute the derivatives of $J(\mu)$ with respect to μ. To compute the approximated minimizer $\tilde{\mu}$ of this functional, we implement the following gradient descent method:

- Initialization: Set initial guess μ_0 to be homogenous. Compute the initial forward problem $\mathbf{u}_0 = \mathbf{u}_{\text{mod}}(\mu_0)$, the initial cost function $||\mathbf{u}_{\text{exp}} - \mathbf{u}_0||_2^2$, the initial adjoint problem $\mathbf{v_0}$, and set the initial descent parameter δ_0.
- Main loop: For a certain number of iterations N: The direct and adjoint problems being solved at the step $n-1$, denoted by $\mathbf{u}_n = \mathbf{u}_{\text{mod}}(\mu_n)$ and $\mathbf{v}_n$, compute the gradient $\mathbf{e}(\mathbf{u}_n) : \mathbf{e}(\mathbf{v}_n)$. Compute the new forward and adjoint fields $\mathbf{u}_{n+1}$, $\mathbf{v_{n+1}}$, associated to $\mu_{n+1} = \mu_n + \delta_n \mathbf{e}(\mathbf{u_n}) : \mathbf{e}(\mathbf{v_n})$. Compute the new cost functional $J_{n+1} = ||\mathbf{u}_{\text{exp}} - \mathbf{u}_{n+1}||_2^2$.

  If $J_{n+1} < J_n$ then set $\delta_{n+1} = \delta_n * (1.1)$ and $\mu_{n+1} = \mu_{n+1}$;

  If $J_{n+1} > J_n$ then set $\delta_{n+1} = \delta_n * (0.5)$ and $\mu_{n+1} = \mu_n$.
- End: End the loop after a fixed number of iterations, or when the cost becomes smaller than a given parameter ϵ.

Notice that we used an "adaptive" step amplitude δ to enforce the decrease of the functional by decreasing the step. When the descent seems to be efficient, one increases the step size. Although some aspects of the solution are used conventionally, we still observed a significant speed up of the descent. We think of speeding up the method with Newton or Quasi Newton methods, but this remains to be implemented.

2.5. Numerical Illustration

To solve at each iteration the direct and adjoint problems, we used the "SOL" FEM solver developed by the third author [1]. This code solves the incompressible elasticity equation (2.1), using a penalization to ensure the free-divergence condition. We implemented 2D examples on rectangular meshes of rectangular elements. We typically used 140×140 meshes and each computation (forward or adjoint) took approximately 20 seconds on a dual core processor. The "experimental" field obtained numerically is shown in Figure 2.1, together with the reconstruction results. The decrease of the discrepancy functional is described in Figure 2.2.

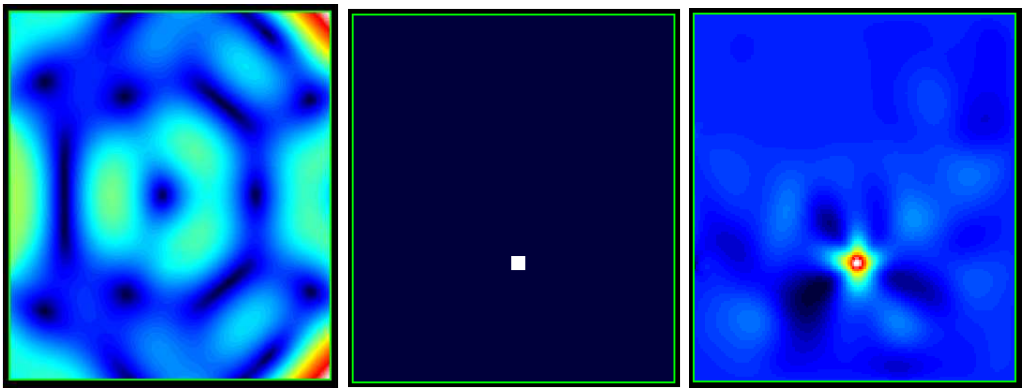

Fig. 2.1. The numerically simulated displacement field on the left, the actual shear modulus map in the middle, and the reconstructed map on the right.

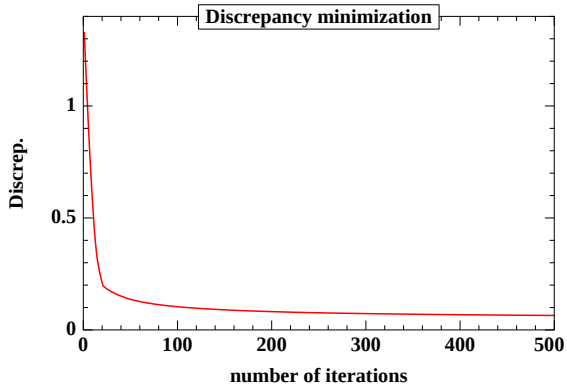

Fig. 2.2. Minimization of the discrepancy functional. We use an adaptive step size in order to enforce the decrease of the functional.

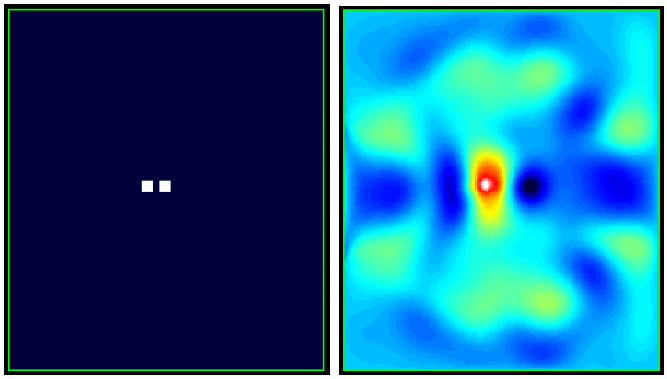

Fig. 2.3. Actual and recovered distributions in the case of a complex map. We fail to recover accurately the details from the far-field measurements.

2.6. Recovery of Details

Suppose we want to recover a more complex map, like a small anomaly of different shear modulus $\tilde{\mu}$, of complex shape in a homogenous background of shear modulus μ. Such a situation,

similar to the one encountered in Figure 2.3, corresponds to the scheme in Figure 3.1. To do this task, the algorithm seems to be less efficient, as shown in Figure 2.3. The reason for this is that the information contained in the far-field and in the near-field is completely different because of the diffraction property of the wave propagation. By "near-field" we mean $\mathbf{u}_{\exp}(x)$ for x lying in a neighborhood of the anomaly (denoted W in Figure 3.1). By "far-field" we mean $\mathbf{u}_{\exp}(x)$ for x lying outside of such a neighborhood. It is a fundamental property of the wave equation that the propagation filters all the rapid spatial oscillations in the far-field [14, 15].

This can be seen by decomposing in spherical harmonics the solution $\mathbf{w}(\mathbf{r}, \theta)$ of the Helmholtz equation $(\Delta + \omega^2)\mathbf{w} = 0$ in 2D, scattered from a complex object, and subject to the radiation condition:

$$\mathbf{w}(r, \theta) = \sum \mathbf{w}_n H_n(\omega r) e^{in\theta},$$

where H_n are Hankel functions. The rapid angular oscillations associated with high values of n, are associated to rapidly decaying H_n. The relevant parameter that quantifies this decay is ωr, which means that the characteristic decay length is determined by the wavelength $\Lambda = \frac{2\pi}{\omega}$.

Thus the algorithm performs a trade-off between the far-field reconstruction, that is the reconstruction from the information lying in the far-field and the near-field reconstruction, which uses the information lying in the near-field. In fact, one could decompose the discrepancy functional over the all domain into two parts:

$$J(\mu) = \sum_{\text{near-field}} \frac{1}{2}|\mathbf{u}_{\exp} - \mathbf{u}_{\text{mod}}|^2 + \sum_{\text{far-field}} \frac{1}{2}|\mathbf{u}_{\exp} - \mathbf{u}_{\text{mod}}|^2.$$

But these two parts have different minimizers, for, as said already, the intrinsic reason that the information carried in the near- and far-field parts of $\mathbf{u}_{\exp}$ are different.

As shown in [4], the only information that travels away from the anomaly is the viscous moment tensor and the reconstructed anomaly should be an equivalent ellipse (See Figure 2.3 for an illustration of this). But in the near-field, the perturbation is the solution of a problem which is well-posed in the sense that the near-field is one-to-one with the corresponding shape and contrast of the anomaly.

For this reason, we want to separate the two scales in order to coherently treat each part of the information.

3. Scale Separation in Solving the Inverse Problem

We introduce two scales in the problem as illustrated in Figure 3.1. The small spatial scale is associated with a rapid variable $\xi = (x - z)/\epsilon$. It characterizes the perturbation due to the anomaly in a small region around z. The slow variable is associated to perturbations far from the anomaly.

As shown in [4], there is no asymptotic development of the perturbed displacement field which is valid for all the domain Ω, that is why we have developed a two-scale model. As the perturbation parameter ϵ goes to 0, we have introduced an ansatz development for the

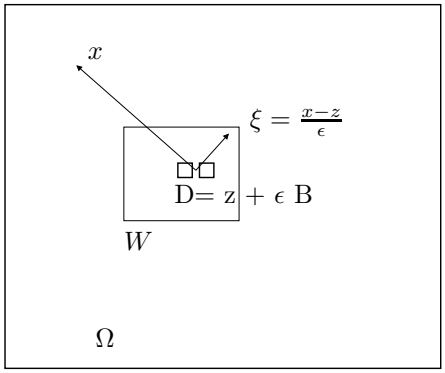

Fig. 3.1. We introduce two scales to capture the different natures of the perturbations near and far from the anomaly.

perturbed elastic field. Assuming that $\mathbf{u}$ is the displacement part of the solution $(\mathbf{u}, p)$ to

$$\begin{cases} (\mu\Delta + \omega^2\rho)\mathbf{u} + \nabla p = 0 \quad \text{in } \Omega - \overline{D}, \\ (\tilde{\mu}\Delta + \omega^2\rho)\mathbf{u} + \nabla p = 0 \quad \text{in } D, \\ \mathbf{u}|_- = \mathbf{u}|_+ \quad \text{on } \partial D, \\ (p|_+ - p|_-)\mathbf{N} + \mu\frac{\partial \mathbf{u}}{\partial \mathbf{N}}|_+ - \tilde{\mu}\frac{\partial \mathbf{u}}{\partial \mathbf{N}}|_- = 0 \quad \text{on } \partial D, \\ \nabla \cdot \mathbf{u} = 0 \quad \text{in } \Omega, \\ \mathbf{u} = F \quad \text{on } \Gamma_1, \\ p\nu + \mu\frac{\partial \mathbf{u}}{\partial \nu} = 0 \quad \text{on } \Gamma_2, \end{cases} \tag{3.1}$$

where $\frac{\partial}{\partial \mathbf{N}}$ denotes $\frac{1}{2}(\frac{\partial}{\partial \mathbf{n}} + \frac{\partial}{\partial \mathbf{n}}^t)$ and $\mathbf{n}$ is the outward unit normal to ∂D, we have set the following *a priori* inner and outer expansions, that correspond to the perturbed near- and far-fields:

$$\begin{cases} \mathbf{u}(x) = U_0(x) + \epsilon U_1(x) + \epsilon^2 U_2(x) + \dots \\ \\ \hat{\mathbf{u}}(\xi) = \mathbf{v}_0(\xi) + \epsilon \mathbf{v}_1(\xi) + \epsilon^2 \mathbf{v}_2(\xi) + \dots \\ \\ \lim\limits_{x \to 0} \mathbf{u}(x) = \lim\limits_{|\xi| \to \infty} \hat{\mathbf{u}}(\xi). \end{cases} \tag{3.2}$$

The same kind of expansions for the pressure field p, which we omit because we are primarily considering the displacement field $\mathbf{u}$, holds.

By plugging in this ansatz in equation (3.1) and making the change of variables $x \to \frac{x-z}{\epsilon}$, one can see, after identifying the terms in ϵ^{-2} and ϵ^{-1}, that

$$\hat{\mathbf{u}}(\xi) = \mathbf{U}_{\mu=\tilde{\mu}}(z) + \epsilon \hat{\mathbf{v}}(\xi) + \mathcal{O}(\epsilon^2),$$

where $\hat{\mathbf{v}}$ is the displacement part of the pair $(\hat{\mathbf{v}}, \hat{p})$ defined by

$$\begin{cases} \mu\Delta\hat{\mathbf{v}} + \nabla\hat{p} = 0 & \text{in } \Omega - \overline{D}, \\ \tilde{\mu}\Delta\hat{\mathbf{v}} + \nabla\hat{p} = 0 & \text{in } D, \\ \hat{\mathbf{v}}|_- = \hat{\mathbf{v}}|_+ & \text{on } \partial D, \\ (\hat{p}|_+ - \hat{p}|_-)\mathbf{N} + \mu\frac{\partial \hat{\mathbf{v}}}{\partial \mathbf{N}}|_+ - \tilde{\mu}\frac{\partial \hat{\mathbf{v}}}{\partial \mathbf{N}}|_- = 0 & \text{on } \partial D, \\ \nabla \cdot \hat{\mathbf{v}} = 0 & \text{in } \Omega, \end{cases} \tag{3.3}$$

subject to the matching conditions:

$$\begin{cases} \hat{\mathbf{v}}(\xi) - \nabla \mathbf{U}_{\mu=\tilde{\mu}}(z)\xi \to 0 & as \quad |\xi| \to \infty, \\ \hat{p}(\xi) \to 0, & as \quad |\xi| \to \infty, \end{cases} \tag{3.4}$$

which couple the inner and outer expansions. Condition (3.4) corresponds to

$$\lim_{x \to z} \mathbf{u}(x) = \lim_{|\xi| \to \infty} \hat{\mathbf{u}}(\xi).$$

For the far-field asymptotic expansion, the difference between the perturbed field and the background field $\mathbf{U}_0$ (associated to the pressure field q_0) satisfies the following system:

$$\begin{cases} (\Delta + \kappa^2)(\mathbf{u} - \mathbf{U}_0) + \dfrac{1}{\mu}\nabla(p - q_0) = 0 \quad \text{in } \Omega \setminus \overline{D}, \\ (\Delta + \kappa^2)(\mathbf{u} - \mathbf{U}_0) + \dfrac{1}{\mu}\nabla(p - q_0) = (\kappa^2 - \tilde{\kappa}^2)\mathbf{u} + \left(\dfrac{1}{\mu} - \dfrac{1}{\tilde{\mu}}\right)\nabla p \quad \text{in } D, \\ (\mathbf{u} - \mathbf{U}_0)\big|_+ - (\mathbf{u} - \mathbf{U}_0)\big|_- = 0 \quad \text{on } \partial D, \\ \dfrac{1}{\mu}(p - q_0)\big|_+ \mathbf{N} + \dfrac{\partial}{\partial \mathbf{N}}(\mathbf{u} - \mathbf{U_0})\big|_+ \\ \quad = \dfrac{1}{\mu}(p - q_0)\big|_- \mathbf{N} + \dfrac{\partial}{\partial \mathbf{N}}(\mathbf{u} - \mathbf{U_0})\big|_- + \dfrac{\tilde{\mu} - \mu}{\mu}\dfrac{\partial \mathbf{u}}{\partial \mathbf{N}}\big|_- \quad \text{on } \partial \mathbf{D}, \\ \nabla \cdot (\mathbf{u} - \mathbf{U}_0) = 0 \quad \text{in } \Omega, \\ \mathbf{u} - \mathbf{U}_0 = 0 \quad \text{on } \partial\Omega, \end{cases} \tag{3.5}$$

where $\kappa = \rho\omega/\mu$ and $\tilde{\kappa} = \rho\omega/\tilde{\mu}$. Integrating over $y \in \Omega \setminus \overline{D}$ the first equation in (3.5) against the Green function $\mathbf{G}^i(x, y)$, which is defined by

$$\begin{cases} \left(\Delta_y + \frac{\omega^2 \rho}{\mu}\right) \mathbf{G}^i(x, y) + \nabla \pi = \delta_{y=x} \mathbf{e_i}, \\ \nabla_y . \mathbf{G}^i(x, y) = 0, \end{cases} \tag{3.6}$$

and using the divergence theorem, we have obtained the following representation formula for $x \in \Omega$:

$$\mathbf{u}(x) = \mathbf{U}_0(x) + \left(\frac{\tilde{\mu}}{\mu} - 1\right) \int_{\partial D} \mathbf{G}(x, y) \frac{\partial \mathbf{u}}{\partial \mathbf{N}}\bigg|_- (y)\, d\sigma(y) + \left(\frac{1}{\mu} - \frac{1}{\tilde{\mu}}\right) \int_D \mathbf{G}(x, y) \nabla p(y)\, dy,$$

where $\mathbf{GX} = \sum_{i,j} \mathbf{e}_i \mathbf{G}^i_j \mathbf{X}_j$ and $\mathbf{G}^i_j$ is the j-th component of $\mathbf{G}^i$. Since

$$\left(\frac{\tilde{\mu}}{\mu} - 1\right) \int_{\partial D} \frac{\partial \mathbf{u}}{\partial \mathbf{N}}\bigg|_- (y)\, d\sigma(y) + (\frac{1}{\mu} - \frac{1}{\tilde{\mu}}) \int_D \nabla p(y)\, dy = -\left(\frac{\tilde{\mu}}{\mu} - 1\right) \kappa^2 \int_D \mathbf{u}\, dy,$$

as it can be seen by integration by parts, we obtain from the inner expansion that for x far away from z, in $\mathbb{R}^2$,

$$\begin{aligned} \mathbf{u}_0(x) \approx \mathbf{U}_0(x) + \epsilon^2 \sum_{i,j,\ell=1}^{2} \mathbf{e}_i \partial_\ell \mathbf{G}^i_j(x, z) \Bigg[(\frac{\tilde{\mu}}{\mu} - 1) \int_{\partial B} \left(\frac{\partial \hat{\mathbf{v}}}{\partial \mathbf{N}}\right)_j \Bigg|_- (\xi) \xi_\ell\, d\sigma(\xi) \\ + \left(\frac{1}{\mu} - \frac{1}{\tilde{\mu}}\right) \int_B \partial_j \hat{p}(\xi) \xi_\ell\, d\xi \Bigg]. \end{aligned}$$

which may be simplified as follows:

$$\mathbf{u}_0(x) \approx \mathbf{U}_0(x) + 2\epsilon^2(\frac{\tilde{\mu}}{\mu} - 1) \sum_{i,j,\ell=1}^{2} \mathbf{e}_i \partial_\ell \mathbf{G}^i_j(x,z) \Big[\int_B \mathbf{e}(\hat{\mathbf{v}})_{j,\ell}(\xi)\, d\sigma(\xi) \Big],$$

where $\mathbf{e}$ is defined in (2.1).

The quantity $\int_B \mathbf{e}(\hat{\mathbf{v}})_{j,\ell}(\xi)\, d\sigma(\xi)$ is given in terms of the viscous moment tensor $(V^{p,q}_{j,\ell})_{j,\ell,p,q}$, defined in [4], by

$$\mathbf{V}(B)_{j,\ell} = \int_B \mathbf{e}(\hat{\mathbf{v}})_{j,\ell}(\xi)\, d\sigma(\xi) = \partial_p \mathbf{U}^q_0 V^{p,q}_{j,\ell}.$$

These asymptotics can be summarized as follows:

$$\begin{cases} \hat{\mathbf{u}}(\xi) \approx \mathbf{U}_{\mu=\tilde{\mu}}(z) + \epsilon\, \hat{\mathbf{v}}(\xi) & \text{in the near-field,} \\ \\ \mathbf{u}(x) \approx \mathbf{U}_{\mu=\tilde{\mu}}(x) + \epsilon^2(\frac{\tilde{\mu}}{\mu} - 1)\nabla\mathbf{G} : \mathbf{V}(B) & \text{in the far-field.} \end{cases} \tag{3.7}$$

Here, $\nabla\mathbf{G} : \mathbf{V}$ is a compact notation for $\mathbf{e}_i \partial_\ell \mathbf{G}^i_j \mathbf{V}(B)_{j,\ell}$. We stress the following points:

- Although the perturbation in the displacement field decays rapidly with the volume of the defect, there exists a coupling between a local perturbation at the location z and the far-field everywhere in the domain.
- As expected, the far-field perturbation carries a less accurate information since the field $\hat{\mathbf{v}}$ is integrated over the boundary of B and it is multiplied by $\nabla\mathbf{G}$, whereas the near-field carries a more accurate information.
- The fact that there is no uniform asymptotics for the perturbed field over the whole domain, shows that it is impossible to do accurate inverse processing of the data on the whole domain, one has to perform *local reconstruction*. We exploit this fact by running the method on a subregion just around the suspected defect.

In the case of two anomalies, by minimizing the discrepancy functional on a small window W, we can treat coherently the near-field information and achieve a well resolved reconstruction; see Figure 3.2. We conclude that scale separation increases the performance of the method. From the optimization point of view, we observed that the standard gradient method on the whole domain did not converge well toward the real solution μ^*. Using the scale separation method allowed us to achieve better convergence to the true minimizer μ^*. To further illustrate this, Figure 3.3 shows the values of the discrepancy functional at the first iteration and after 100 ones (typical number of iterations when the algorithm converges). Note that the residual discrepancy is located around the anomaly. This residual error cannot be treated on the whole domain because each local modification of the map μ would cause propagation of the error in the whole domain and thus would increase the discrepancy. There is a natural comparison to be made with a Pareto-optimum. One could not decrease the "near-field" error without causing, through the coupling $\epsilon^2(\frac{\tilde{\mu}}{\mu} - 1)\nabla\mathbf{G} : \mathbf{V}$, an equivalent increase in the "far-field" error.

This technique however allows us to bypass this scale coupling obstacle to further decrease the functional, and reach a more accurate minimizer. So, by analyzing the basic properties of equation (2.1), we achieved a better convergence of the minimization algorithm.

Computing the shape derivative of the discrepancy functional on W, we find that $d_{\mathcal{S}}J$ has the following form [3]:

$$d_{\mathcal{S}}J = \mathcal{V}[\mathbf{e}(\mathbf{u}_{\text{mod}})] : \mathbf{e}\Big(\int_W \mathbf{G}(\overline{\mathbf{u}_{\text{mod}} - \mathbf{u}_{\text{exp}}}) \Big),$$

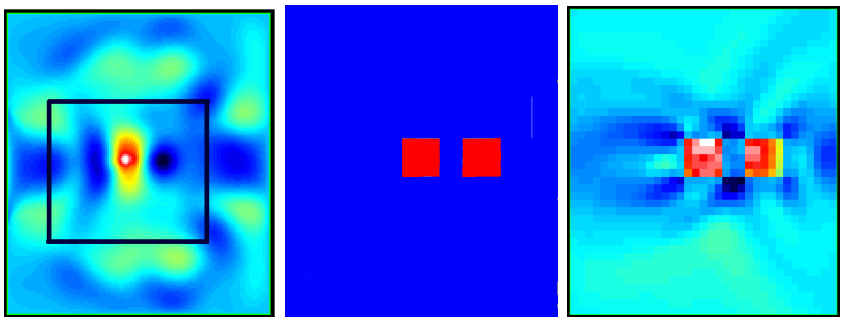

Fig. 3.2. Reconstruction without separation of scales on the left, a zoom on the anomaly that we are trying to recover in the middle, and on the right the reconstruction limited on the subregion defined by the boxed region on the left.

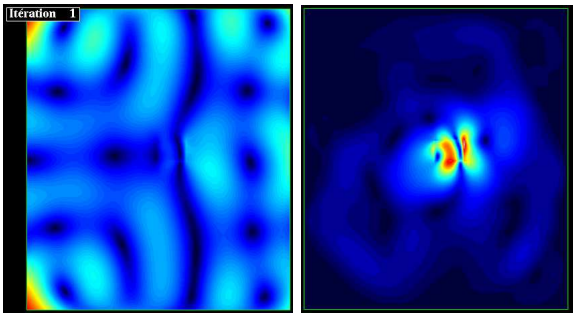

Fig. 3.3. The discrepancy functional at the first iteration (left) and after 100 iterations (right). The residual discrepancy is located around the anomaly.

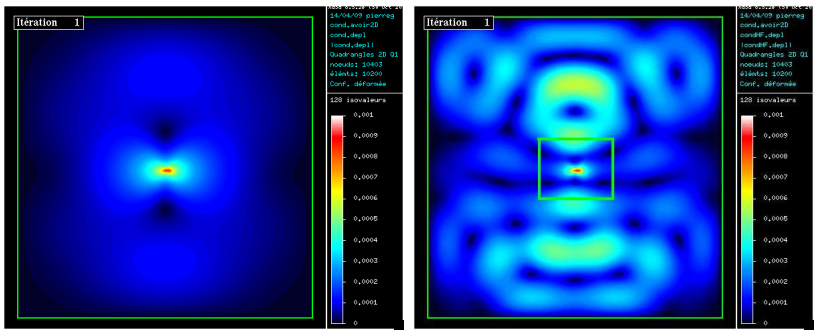

Fig. 3.4. Oscillations in the Dirichlet Green function $\mathbf{G}$ in a window W of size of order of the wavelength (on the left) and much larger than the wavelength (on the right).

where $\mathbf{G}$ is the Dirichlet Green function in the window W and $\mathcal{V}[\mathbf{e}(\mathbf{u}_{\text{mod}})]$ is a viscosity matrix defined at any point on the boundary of the anomaly. Therefore, smaller W, higher the oscillations in $\mathbf{G}$ and better the resolution in reconstruction the anomaly. See Figure (3.4). However, it becomes unstable for finite signal-to-noise ratio in the measurements. This stability issue is the topic of the next section.

4. Stability of the Reconstruction Method

The previous section tends to show that performing local reconstruction allows perfect reconstruction, for a specific sampling of the data. As previously mentioned for the analytical reconstruction,

$$\tilde{\mu} = \frac{\rho\omega^2 \nabla \times \mathbf{u}_{\exp}}{\Delta\nabla \times \mathbf{u}_{\exp}},$$

stability is a crucial issue in practice. So we want to test the stability behavior of our proposed approach. Stability analysis is in general a challenging problem because little is known about the noise structure, yet different noise models give different stability behaviors. We face in this paper the same difficulties, and we merely test the robustness of our method to a perturbation of the data with the following form:

$$\text{For each pixel } X_i \quad \mathbf{u}_{\exp}(X_i) \to \mathbf{u}_{\exp}(X_i) + \frac{\delta}{\mathbf{u}_{MAX}}\mathbf{Y}_i = \mathbf{u}^n_{\exp}(X_i),$$

where $\mathbf{Y}_i$ are gaussian random variables of unitary variance, δ is an amplitude parameter, $\mathbf{u}_{MAX}$ is the maximum amplitude of $\mathbf{u}_{\exp}$. We run our reconstruction method on the noisy sets $\mathbf{u}^n_{\exp}$.

4.1. Stability of the "Global" Reconstruction Method

When we reconstructed the shear modulus from the data from the whole domain Ω (that is without scale separation), we observed that the method was robust as it can be seen in Figure 4.1, where we tried to recover an anomaly of different shear modulus in a homogenous background. This stability feature is due to the fact that the spatial frequencies which dominate in the data are not too high. If we define the wavelength λ by $\sqrt{\frac{\mu}{\rho\omega^2}}$, then we can assume that for smooth media the signal $\mathbf{u}_{\exp}$ in the far-field has mostly spatial frequencies of the order of $k = 1/\lambda$. On the other hand, the noise is uncorrelated and has a broad distribution across the spatial spectrum. The signal-to-noise ratio (SNR) is high in the framework of the global reconstruction. The algorithm is thus marginally disturbed by the noise. This causes the efficient noise to be reduced and the problem to be better posed in the sense of stability.

4.2. Instability of the Local Reconstruction Method

We performed the same test with the near-field reconstruction, on the model example of Figure 3.2. We aim to investigate the stability of the separation of scales when the data is noisy. We observed that the method was unstable if it uses the local data. This was because the fine information of the local data has a high spatial frequency and consequently the information is significantly disturbed by the noise. This means that the SNR is largely affected in this situation. In Figure 4.2, we can see that even with a little noise, we cannot recover the two anomalies. The reconstruction is unstable and gives no information about the shear modulus of the medium.

We investigated the possibility of regularization to recover the stability of the local technique. Instead of minimizing the discrepancy functional over the local domain W, we minimized a regularized functional (see [6]):

$$J_{\text{reg}}(\mu) = J(\mu) + \beta \int_\Omega |\nabla\mu(x)|dx,$$

which depends on a regularization parameter β. To compute the gradient of this functional, one only needs to modify the technique described in Section 2.3 by adding the derivative with respect to μ of the regularization term. The gradient of the regularization term, which is the

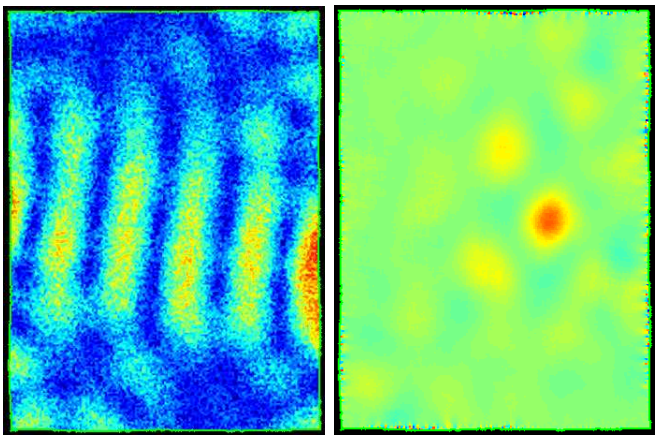

Fig. 4.1. Elastic field with 35 % noise, and reconstruction of an anomaly. Although the data is seriously noisy, the anomaly is still visible.

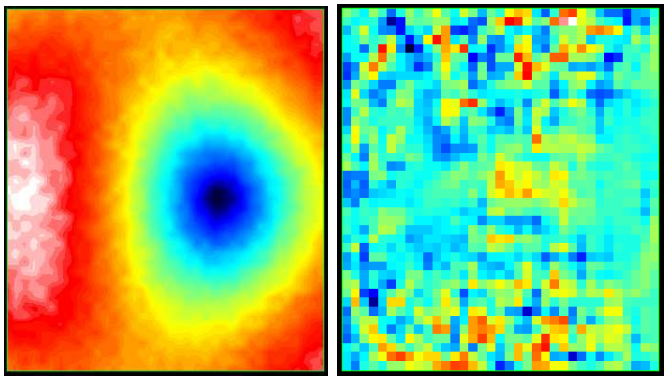

Fig. 4.2. Noisy displacement field (local data), and reconstruction pattern with 5% noise: the reconstruction crashes.

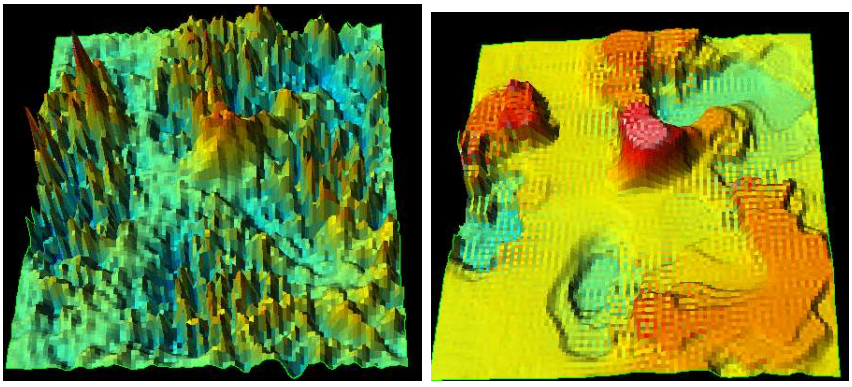

Fig. 4.3. Local reconstruction of an anomaly without regularization (left) and with regularization (right). The anomaly in more visible with the regularized reconstruction.

total variation of the shear modulus map, is given by

$$\frac{\partial TV(\mu)}{\partial \mu} = -\int_\Omega \nabla \cdot (\frac{\nabla \mu}{|\nabla \mu|}) dx.$$

Then, applying the same numerical algorithm with a homogenous initial guess μ_0 and an initial updating step δ_0, we implemented this modified gradient descent method and obtained the results of Figure 4.3. We tried in this example to recover a disk-shaped anomaly located at the center of the domain. We observed that the distribution recovered with the regularization term is indeed smoothed (in the sense of total variation) and the anomaly is visible, whereas it was completely invisible in the classical reconstruction. However, this regularization technique has some drawbacks. Its application is limited if there is no prior knowledge of the smoothness of the target to recover (tumors, pathologies). Moreover, setting the values of δ_0 and β is a sensitive task. If the regularization parameter is too high, the numerical solution of the inverse problem $\tilde{\mu}$ will be homogenous and gives no information about the medium, while if there is not enough regularization, the reconstruction becomes unstable. Finally, setting these parameters is data-dependent, which limits its practical applications.

4.3. Resolution Performance of the Algorithm

We discuss now the resolution performance of our technique: given a specific data set $\mathbf{u}_{\text{exp}}$, how accurately does our technique recover μ^* ? If we assume that we have no noise in the data and that the sampling density is infinite, which means we know the value of the displacement in each point of Ω, then we can perfectly reconstruct the shear modulus map.

Indeed, as explained in [4], with perfect data, one could scale the local data and the problem would be reduced to solving an inverse problem for the Stokes equation, namely problem (3.3) in Section 3. We have a unique solution for this problem. Moreover, our numerical method is efficient; cf. Figure 3.2. Thus with infinite SNR, infinite sampling density, the resolution is also infinite; we could recover perfectly the map μ^*.

In practice, the data is noisy and acquired on a finite number of points in the domain Ω. This changes the performance one could expect when one solves the elastography inverse problem. If one acquires enough points per wavelength, and have infinite SNR, one can recover the map μ with the same accuracy as the sampling. The reconstruction is still accurate, since one can still use the scale separation technique.

The most important problem arises when some noise is added to the data, since the scale separation technique becomes unstable in this case. There is a trade-off between accuracy and stability. The global optimization method applied to the entire domain is stable but not accurate. On the other hand, the local method is accurate but unstable.

We have to choose a window that is not so small to preserve some stability and not so big so that we can gain some accuracy. In the presence of noise, the loss of accuracy due to the scale coupling is thus inevitable. The resolution of the algorithm is therefore limited in the noisy data case. The question is to quantify this limit: what is the critical size of the window W that switches between far-field and near-field reconstructions ?

In practice, the critical size is of order of the wavelength λ. However, it is unclear exactly how far from an arbitrary shaped object would the near-field still be dominant over the far-field. It is important to underline that the size of W is *frequency dependant*, especially when it comes to study the frequency dependance of μ^*, which is of clinical relevance.

In the finite difference methods used in [18], which exploit the formula $\mu = \rho\omega^2 q/\Delta q$ (see Section 2), the data has to be smoothed to compute its derivatives in a stable manner. This is achieved with a low-pass spatial filter that has a cut-off frequency, which can be interpreted in terms of the spatial dimension W_{cut}. If W_{cut} is too small, then the filter does not smooth enough and the algorithm is unstable while if W_{cut} is too high, then the smoothing is drastic and it kills the relevant information. This is the same trade-off in our scale separation technique. So both techniques are *semi-local* in practice. Therefore, one needs to carefully analyze the spatial spectrum of the data.

5. Conclusion and Perspectives

In this paper we have implemented an optimization technique in order that solves the inverse problem in MRE. We have presented the scale separation technique, which is inspired by the rigorous asymptotic expansion for the perturbations in the elastic field that are due to an anomaly. We have discussed the numerical results of this technique, and compared their intrinsic properties to existing methods. Further work to quantify the window size W should allow us to be more quantitative about the performance of the proposed reconstruction techniques in elastography.

Acknowledgments. This work was partially supported by the ANR project EchoScan (AN-06-Blan-0089).

References

[1] G. Allaire, F. Jouve, and A.M. Toader, Structural optimization using sensitivity analysis and a level-set method, *J. Comput. Phys.*, **194** (2004), 363-393.

[2] H. Ammari, An Introduction to Mathematics of Emerging Biomedical Imaging, Mathématiques et Applications, Vol. 62, Springer-Verlag, Berlin, 2008.

[3] H. Ammari, P. Garapon, F. Jouve, and H. Kang, A new optimal control approach for the reconstruction of extended inclusions, *J. Differ. Equations*, to appear.

[4] H. Ammari, P. Garapon, H. Kang, and H. Lee, A method of biological tissues elasticity reconstruction using magnetic resonnance elastography measurements, *Quart. Appl. Math.*, **66** (2008), 139-175.

[5] J. Bercoff, M. Tanter, and M. Fink, Supersonic shear imaging: a new technique for soft tissues elasticity mapping, *IEEE Trans. UFFC.*, **51** (2004), 374-409.

[6] T.F. Chan and X.-C. Tai, Level set and total variation regularization for elliptic inverse problems with discontinuous coefficients, *J. Comput. Phys.*, **193** (2003), 40-66.

[7] T. Deffieux, J.L. Genisson, A. Nordez, M. Tanter, and M. Fink, Ultrafast imaging of in vivo muscle contraction using ultrasound, *Appl. Phys. Lett.*, **89** (2006).

[8] V. Girault, P.A. Raviart, Finite Elements Methods for Navier-Stokes Equations, Springer, New York, 1986.

[9] J.F. Greenleaf, M. Fatemi, and M. Insana, Selected methods for imaging elastic properties of biological tissues, *Annu. Rev. Biomed. Eng.*, **5** (2003), 57-78.

[10] L. Huwart, F. Peeters, R. Sinkus, L. Annet, N. Salameh, LC. Ter Beek, Y. Horsmans, and BE. Van Beers, Liver fibrosis: non invasive assessment with MR Elastography, *NMR Biomed*, **19** (2006).

[11] F. Ihlenburg, Finite Elements Analysis of Acoustic Scattering, Springer, New York, 1998.

[12] B. Jadamba, A.A. Khan, and F. Raciti, On the inverse problem of identifying Lamé coefficients in linear elasticity, *Comput. Math. Appl.*, **56** (2008), 431-443.

[13] O. A. Ladyzhenskaya, The Mathematical Theory of Viscous Incompressible Flow, 2nd English Edition, Gordon and Breach, New York, 1969.

[14] P. Maponi, L. Misici, and F. Zirilli, Three-dimensional time harmonic inverse electromagnetic scattering, Inverse problems in mathematical physics, 139-147, Lecture Notes in Phys., 422, Springer, Berlin, 1993.

[15] L. Misici and F. Zirilli, Three-dimensional inverse obstacle scattering for time harmonic acoustic waves: a numerical method, *SIAM J. Sci. Comput.*, **15** (1994), 1174-1189.

[16] R. Muthupillai, D.J. Lomas, P.J. Rossman, J.F. Greenleaf, A. Manduca, and R.L. Ehman, Magnetic resonance elastography by direct visualization of propagating acoustic strain waves, *Science*, **269** (1995), 1854-1857.

[17] R. Sinkus, J. Lorenzen, D. Schrader, M. Lorenzen, M. Dargatz, and D. Holz, High-resolution tensor MR elastography for breast tumour detection, *Phys. Med. Biol.*, **45** (2000), 1649-1664.

[18] R. Sinkus, M. Tanter, S. Catheline, J. Lorenzen, C. Kuhl, E. Sondermann, and M. Fink, Imaging anisotropic and viscous properties of breast tissue by magnetic resonance-elastography, *Magn. Reson. Med.*, **53** (2005), 372-387.

[19] E.E.W. Van Houten, K.D. Paulsen, M.I. Miga, F.E. Kennedy, and J.B. Weaver, An overlapping subzone technique for MR-Based elastic property reconstruction, *Magn. Reson. Med.*, **42** (1999), 779-786.

[20] E.E.W. Van Houten, M.M. Doyley, F.E. Kennedy, J.B. Weaver, and K.D. Paulsen, Initial in vivo experience with steady-state subzone-based MR elastography of the human breast, *J. Magn. Reson. Imaging.*, **17** (2000), 72-85.